Astron. Astrophys. 326, 305–317 (1997)

ASTRONOMY AND ASTROPHYSICS

Circumstellar dust shells around long-period variables

V. A consistent time-dependent model for the extreme carbon star AFGL 3068

J.M. Winters[1], **A.J. Fleischer**[1], **T. Le Bertre**[2], **and E. Sedlmayr**[1]

[1] Technische Universität Berlin, Institut für Astronomie und Astrophysik, Sekr. PN 8-1, Hardenbergstr. 36, D-10623 Berlin, Germany
[2] DEMIRM, Observatoire de Paris, 61, av. de l'Observatoire, F-75014 Paris, France

Received 22 November 1996 / Accepted 29 April 1997

Abstract. We present a consistent time–dependent model for the extreme carbon star AFGL 3068. The model includes a consistent treatment of the interactions among hydrodynamics, thermodynamics, dust formation, and chemistry. It is determined by the stellar parameters of the initial hydrostatic model: stellar mass $M_\star$ = 1 $M_\odot$, stellar luminosity $L_\star$ = 1.3 10^4 $L_\odot$, stellar temperature $T_\star$ = 2200 K, and carbon–to–oxygen abundance ratio ϵ_C/ϵ_O = 1.38. The pulsation of the star is simulated by a piston approximation at the inner boundary where the velocity varies sinusoidally with a period of P = 696 d and an amplitude of Δu = 8 km s^{-1}. This model yields a time averaged outflow velocity of 14.7 km s^{-1} in good agreement with the rather well determined observed value and an average mass loss rate of 1.2 10^{-4} $M_\odot$yr^{-1} which is about a factor of 4 larger than the value usually derived from the fitting of CO rotational lines profiles. Based on the atmospheric structure resulting from this hydrodynamic calculation, we have performed angle– and frequency–dependent continuum radiative transfer calculations, which yield the spectral energy distributions at different phases of the pulsation cycle, synthetic light curves at different wavelengths and synthetic brightness profiles of the dust shell model. The computed energy distributions and the synthetic light curves are in good agreement with the observations of AFGL 3068. We derive a distance to AFGL 3068 of 1200 parsec. Furthermore, properties of the resulting grain size distribution function are discussed. The dominant size of the grains formed in the circumstellar shell is found to be $< a > \sim 0.1\mu$m but grains with radii up to 0.7μm are also formed in such a quantity that they may contribute significantly to light scattering in the near–infrared.

We propose to perform high–resolution spatial observations of the circumstellar dust shell around AFGL 3068 which could be compared with the predictions of the model calculation.

Key words: hydrodynamics – radiative transfer – stars: carbon – circumstellar matter – stars: late–type – stars: individual: AFGL 3068

Send offprint requests to: J.M. Winters
e-mail: Winters@physik.TU-Berlin.DE

1. Introduction

Carbon stars on the Asymptotic Giant Branch (AGB) may undergo mass loss. The contribution of these stars to the replenishment of the Interstellar Medium (ISM) is uncertain but could be of the order of 0.5 $M_\odot$ yr^{-1} (Epchtein et al. 1990). Whatsoever, they certainly dominate the ISM enrichment in carbon–rich material over WC Wolf–Rayet stars, RV Tauri stars, novae, and supernovae (e.g. Gehrz 1989) and thus play an important rôle in the chemical evolution of the Galaxy. Due to mass loss, these objects are surrounded by envelopes of gas and dust. Their spectra are characterized by an emission feature at 11.3 μm usually ascribed to silicon carbide grains (SiC; Treffers & Cohen 1974). With the advent of Infrared (IR) surveys, unidentified IR sources have been discovered and some have been found to consist of heavily obscured carbon stars. For these extreme carbon stars (ECS), the 11.3 μm feature (henceforth called "SiC feature") may be smoothed by self–absorption or even appear in absorption (Cohen 1984). The large optical depth of these sources points to a process of mass loss at a huge rate ($\dot{M} \geq 10^{-5}$ $M_\odot$ yr^{-1}). They may thus contribute significantly to the supply of carbon–rich material in the ISM (Kastner et al. 1993). By their extreme properties ECS allow to probe the models of carbon dust formation and the significance of dust for the dynamics of the shell. In this context, those ECS for which the SiC feature is in absorption are particularly relevant.

The best studied one is actually AFGL 3068. It is a long–period variable (P$\sim$ 700 days). Its broad band spectrum mimics that of a blackbody at $\sim$ 300 K (Jones et al. 1978). An absorption around 11.3 μm can be seen in its Low Resolution Spectrum (LRS, IRAS Science Team 1986). The detailed observations of Justtanont et al. (1996) show that this feature might in fact be due to SiC. The detection of carbon–rich molecules such as HCN, HC_3N, etc. (Bujarrabal et al. 1994) supports the carbon–rich chemistry of the circumstellar shell. Omont et al. (1993) have shown that a good way of finding such "extreme" ECS is to look in the ζ4 autoclass of Cheeseman et al. (1989). This class is characterized by LRS and IRAS color temperatures, $T_{col} \sim$ 300 K. The ζ4 autoclass is also populated by OH/IR sources

with self–absorbed silicate feature which sometimes can mimic a SiC feature. There are also sources with emission at 8.6 and 11.3 μm ascribed to PAH molecules. The latter appear associated to post–AGB sources. Therefore, other pieces of information are necessary to sort out the mass losing evolved carbon stars. In the near–infrared the extreme ECS have a color index [K–L] ≥ 7. Also, mass losing carbon stars are long–period variables (P$\geq$400 days; Jura 1986). Candidates that could be considered are for instance AFGL 190 ($T_{col} \sim 300$ K; Gehrz & Hackwell 1976) or AFGL 5250 ([K–L] > 7; Fouqué et al. 1992). Nevertheless, for our study we selected AFGL 3068 because it is the brightest and best studied specimen, having the highest known mass loss rate of any carbon rich AGB stars in the solar neighborhood. Also the data available on this source are particularly appropriate to our intended modeling. Finally, its spectral energy distribution has already been modelled by several authors and although they do not treat the dust formation and dust dynamics, their results give useful indications from which to start.

In this paper we present a consistent time–dependent model for the circumstellar dust shell (CDS) around AFGL 3068, including a detailed treatment of hydrodynamics, equilibrium chemistry, formation, growth and evaporation of carbon grains, and radiative transfer. We start with an overview of the existing observational data in Sect. 2, followed by a short description of the modeling method in Sect. 3. The results are presented in Sect. 4 and discussed in Sect. 5. We finish this paper with the conclusions in Sect. 6.

2. The observational data

The source was monitored continuously for a lapse of 4 years in the photometric bands K, L and M (Le Bertre, 1992). A period of 696 days was deduced. The peak to peak amplitude is $\sim$ 1.9 mag in K, $\sim$ 1.4 in L and $\sim$ 1.1 in M. Some irregularities in the light curve shapes can be seen. These features are real and will be discussed further below (see Sect. 4.4). In addition, 10–20 μm photometric data were acquired at 4 phases quasi–simultaneously with K, L and M data (Le Bertre et al. 1995). The sampling is not sufficient to measure the amplitude of the light curves in this wavelength range. However, by forcing a sinewave of period 696 days through the data, one can estimate the peak to peak amplitude at 10 μm, ~ 0.7 mag., and at 20 μm, ~ 0.5. At longer wavelengths, data have been obtained by IRAS (IRAS Science Team 1988) and by Groenewegen et al. (1993). Although these observations were not performed at the same phase as the 2–20 μm ones, they give unique indications on the energy distribution in the 20–1000 μm range. One should note that the Groenewegen et al. data were obtained with a beam of 19 arcsec and probe only the central part of the CDS. On the other hand, the IRAS results were obtained with synthesized beams of 2 arcmin (at 12 μm) to 4 arcmin (at 100 μm) enclosing most of the flux emitted in this wavelength range (see Table 3 in Le Bertre et al. 1995).

The 1–100 μm energy distributions obtained at the 4 different phases by Le Bertre et al. (1995) allow to derive an average bolometric luminosity:

$$<L> \sim 8.2\,10^3 \times d_{kpc}^2\, L_\odot,$$

with peak to peak amplitude, ~ 0.8 mag. If one adopts the period–luminosity relation for Miras derived by Whitelock et al. (1991), the average luminosity should be $\sim 11500\,L_\odot$. This translates to a distance of 1185 pc.

The circumstellar shell was detected also in several molecular lines (Bujarrabal et al. 1994, and references therein). From the CO observations of Knapp & Morris (1985), an expansion velocity of ~ 14.5 km s^{-1} can be deduced. This velocity should correspond to the terminal velocity of the gas. Also, by modeling the CO line profile, the total mass loss rate is found to be

$$\dot{M} \sim 2\,10^{-5} \times d_{kpc}^2\, M_\odot\ yr^{-1}\ .$$

3. The modeling method

The method applied here to model the circumstellar dust shell of AFGL 3068 is a consistent time–dependent treatment of hydrodynamics, thermodynamics, equilibrium chemistry, dust formation, –growth and –evaporation, and radiative transfer.

We consider a spherically symmetric atmosphere surrounding a pulsating red giant, characterized by its mass $M_\star$, effective temperature $T_\star$, luminosity $L_\star$, and the photospheric element abundances ϵ_i. In order to simulate the interior pulsation of the star, we apply a sinusoidal variation of the velocity with amplitude Δu and period P at the inner boundary r_i of the model. Thus, our models are defined by the prescription of the 4 fundamental stellar parameters ($T_\star$, $L_\star$, $M_\star$, ϵ_i) and of (P, Δu) to describe the interior pulsation. Since $T_\star$ and $L_\star$ vary in time during the calculation, in the following we will refer to their values in the hydrostatic initial model as T_0 and L_0. Starting with the hydrostatic initial model, the velocity amplitude of the piston is increased slowly until the maximum value Δu is reached. Due to the sinusoidal variation of the velocity at the inner boundary, the location of r_i itself varies sinusoidally around its rest position $r_0 = r_i(t = 0)$ with amplitude $\Delta r_i = \Delta u\, P/2\pi$. The development of the model is followed in time until a regular pattern of the radial structure is reached. Details of the hydrodynamic modeling and the basic equations are given in Fleischer et al. (1992, henceforth called Paper I).

For the determination of the equilibrium temperature the radiative transfer problem is solved in grey approximation in the *hydrodynamic calculation* (see below), which of course does not yield the spectral energy distribution nor the light curves or the surface brightness profiles of the dust shell model. Therefore, in a second step, we solve the frequency–dependent stationary radiative transfer equation in spherical geometry for given radial structures of the dust shell model, i.e. at fixed instants of time. Details of the radiative transfer calculation are described in Winters et al. (1994a, 1994b). The transfer processes considered are grey absorption and thermal emission of the gas and frequency–dependent absorption and thermal emission of the dust grains assuming the small particle limit of Mie theory. (The validity of this assumption for the present model is discussed in Sect. 5.3).

In the small particle limit, the absorption coefficient of the dust component $\kappa_\nu^{\rm d}$ is expressed by (cf. Gail et al. 1984)

$$\kappa_\nu^{\rm d}(r) = \frac{8\pi^2 a_0^3}{\lambda} {\rm Im}\left\{\frac{m(\nu)^2-1}{m(\nu)^2+2}\right\} K_3(r)\,. \quad (1)$$

The quantity $K_3(r)$ is the third moment of the size distribution function of the dust particles $f(a,r)$ and represents the number density of monomers condensed into grains $n_{\rm c}$. It is defined by

$$a_0^3 K_3 = \int_{a_\ell}^{\infty} a^3 f(a,r) da = a_0^3 n_{\rm c}\,, \quad (2)$$

where a_0 denotes the hypothetical radius of a monomer contained in a dust grain ($a_0 = 1.28\,10^{-8}$ cm for carbon grains), and a_ℓ is a lower limiting size of the dust particles ($a_\ell \approx 10^{-7}$cm), which ensures that the species considered as particles have macroscopic properties (like a surface).

For the calculation presented here, the complex refractive index $m(\nu)$ of the grain material is taken from Maron (1990) which is appropriate for pure amorphous carbon grains.

Three major improvements compared with Paper I have been introduced in the hydrodynamic calculation, which are described in the following:

i) In our previous calculations the stellar temperature $T_\star$ was assumed to remain constant during the temporal evolution of the model, while the stellar luminosity $L_\star(t)$ and the stellar radius $R_\star(t)$ were allowed to vary in time according to the Stefan-Boltzmann law

$$L_\star = 4\pi R_\star^2 \sigma T_\star^4\ . \quad (3)$$

However, there is no physical reason for the stellar temperature to remain constant during the pulsation cycle of the star. Therefore, we now apply a different inner boundary condition, which keeps the radiative flux through the inner boundary $r_{\rm i}$ constant:

$$F(r_{\rm i}) = \frac{L_\star}{4\pi r_{\rm i}^2} = \frac{L_0}{4\pi r_0^2} = {\rm const}(t)\ . \quad (4)$$

As a consequence, the three quantities $L_\star, R_\star, T_\star$ now vary in time according to Eq. (3), where the current values for $R_\star$ and $T_\star$ follow from the consistency requirement Eq. (9). $R_\star$ and $T_\star$ might now be quantities representative of a region in the stellar atmosphere where dust already has formed and might not describe the stellar photosphere. This is the case for the model presented here (see Fig. 1).

ii) The equilibrium temperature, previously determined by the method of Lucy (1971, 1976), is now calculated following Unno & Kondo (1976) in the improved version described in Hashimoto (1995) but still in grey approximation. Applying this method, the radiative equilibrium temperature is given by

$$T_{\rm eq}^4(r) = \frac{1}{\sigma}\frac{1}{2} r_{\rm i}^2 F(r_{\rm i}) \cdot \left[\frac{1}{R^2(1+\mu_{\rm R})} + \frac{\mu_{\rm R}}{R^2} - \frac{\mu_{\rm r}}{r^2} + \frac{3}{2}\int_r^R (\chi_{\rm F} + \frac{2\mu_{r'}}{r'})\frac{dr'}{r'^2}\right] \quad (5)$$

where μ_r is calculated from

$$\frac{{\rm d}\mu_r^3}{{\rm d}r} = \frac{1}{4}\chi_{\rm F}(r)(1-5\mu_r^2) + \frac{3\mu_r}{r}(1-\mu_r^2) \quad (6)$$

with the boundary condition

$$\mu_r(r_{\rm i}) = 0\ . \quad (7)$$

(σ: Stefan–Boltzmann constant, F: radiative energy flux, R: location of the outer boundary, $\chi_{\rm F}$: flux–mean extinction coefficient)

As in our previous calculations, we treat shocks in the isothermal limiting case. Therefore, the gas temperature $T_{\rm g}(r)$ equals the local equilibrium temperature $T_{\rm eq}(r)$ throughout the atmosphere at every instant of time. Since we assume radiative equilibrium, $r^2F(r)$ is constant with respect to r at any given instant of time,

$$r^2 F(r) = \frac{L_\star}{4\pi} = R_\star^2 \sigma T_\star^4\ . \quad (8)$$

Inserting Eq. (8) into Eq. (5) the consistency requirement $T_{\rm eq}(r = R_\star) = T_\star$ demands the implicit condition

$$\left\{\frac{r^2}{2}\left[\frac{1}{R^2(1+\mu_{\rm R})} + \frac{\mu_{\rm R}}{R^2} - \frac{\mu_{\rm r}(r)}{r^2} + \frac{3}{2}\int_r^R (\chi_{\rm F} + \frac{2\mu_{r'}}{r'})\frac{dr'}{r'^2}\right]\right\}_{r=R_\star} = 1 \quad (9)$$

to be fulfilled in order to determine the current value of $R_\star$ (and thus $T_\star$).

This modification in the determination of the temperature structure was necessary for the model presented here since the assumption of an optically thin dust shell, which has to be made for Lucy's approximation to be applicable, is not valid here. As a consequence of the dust shell's optical thickness, the values of $R_\star$ and $T_\star$ resulting from Eq. (9) do not describe the star but rather the circumstellar shell: the "stellar" radius $R_\star$ is located in a region around 6 R_0, where R_0 is the stellar radius of the hydrostatic initial model. The temporal evolution of $R_\star$ and $T_\star$ of the model for AFGL 3068 is shown in Fig. 1 for a time interval of 10 pulsation cycles after the velocity amplitude Δu has reached its specified value. As the inner boundary $r_{\rm i}$ is moving sinusoidally, from Eq. (4) it follows that $L_\star$ also varies sinusoidally. It is evident from Fig. 1, that $R_\star$ essentially reflects the dynamical behavior of the inner part of the dust shell (see also Sect. 4.1).

iii) Since in the *hydrodynamic calculation* the radiative transfer problem is treated in grey approximation, we have to replace the transport coefficients of the gas and of the dust component by appropriate frequency–averaged absorption coefficients $\kappa^{\rm g}$ and $\kappa^{\rm d}$. The gas opacity is approximated by $\kappa^{\rm g}/\rho = 2\cdot 10^{-4}{\rm cm^2 g^{-1}}$ (ρ: mass density) which roughly represents the Rosseland mean gas opacity in the relevant temperature and density range (cf. Bowen 1988).

In contrast to our previous calculations, the dust opacity is derived from tables for the Planck–mean value of the extinction efficiency $(Q/a)_{\rm P}^{\rm ext}(T)$ which were calculated for spherical particles in the small particle limit of Mie theory (i.e. $(Q/a) = Q'$ is independent of a, where a is the particle radius). The flux–mean extinction coefficient $\chi_{\rm F}^{\rm d}$ of the

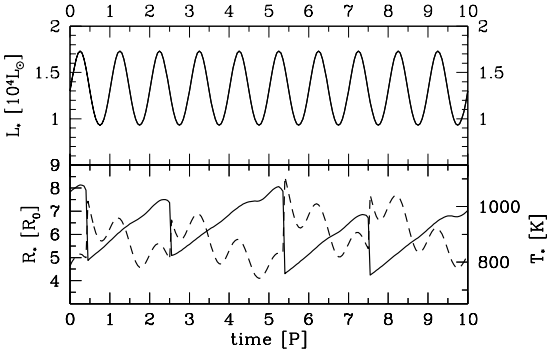

Fig. 1. Temporal variation of stellar luminosity $L_\star$ (upper diagram), "stellar" radius $R_\star$ (solid line, l.h.s. ordinate), and "stellar" temperature $T_\star$ (dashed line, r.h.s. ordinate) resulting from Eq. (9) for the model discussed in Sect. 4

Table 1. Parameters of the initial hydrostatic model

$M_\star$	L_0	T_0	ϵ_C/ϵ_O	P	Δu
$[M_\odot]$	$[L_\odot]$	[K]		[d]	[km s^{-1}]
1.0	$1.3\,10^4$	2200	1.38	696	8

dust component is then approximated by the Planck–mean absorption coefficient κ_P^d:

$$\chi_F^d = \kappa_P^d = \int \pi a^3 (Q/a)_P^{ext} f(a) da = \pi a_0^3 Q_P'^{ext} K_3 \quad . \qquad (10)$$

4. Results

Our best model for AFGL 3068 is determined by the parameters given in Table 1.

The assumed value for the stellar mass of $1M_\odot$ is typical for a carbon star at the lower end of the mass range discussed for these objects. The mass value chosen is consistent with the low outflow velocity measured for AFGL 3068 and its location at a rather high galactic latitude ($|b| = 40.35°$) (cf. Barnbaum et al. 1991).

For the period of 696 d observed for AFGL 3068 (Le Bertre 1992), the period–luminosity relation of Whitelock et al. (1991) yields a luminosity of $11500L_\odot$, whereas Groenewegen & Whitelock (1996) find $10592L_\odot$ for the same period. In the Groenewegen & Whitelock (1996) relation, the uncertainty (1 σ) is estimated to be ~ 0.26 mag. which translates to a luminosity $L_\star$ in the range $8336 - 13457\,L_\odot$. Also, they consider that the luminosity might be underestimated for those sources in their sample which are embedded in a thick circumstellar dust shell. As a consequence, their period–luminosity relation may be biased and may lead to an underestimation of the actual luminosity for the longer period sources (which are also those with the thicker dust shells). In conclusion, the luminosity adopted for our model (13000 $L_\odot$) appears very reasonable for the period of AFGL 3068.

Due to the large obscuration of the star by its CDS, the spectral type of AFGL 3068 has not yet been determined. The stellar temperature of 2200K chosen for the model corresponds to a spectral class C9 (Cohen 1979). From the values adopted for L_0 and T_0 the initial hydrostatic stellar radius, R_0, results as $5.5\,10^{13}$cm = $783R_\odot$.

For the same reason as for the stellar temperature, the photospheric element abundances of AFGL 3068 have not yet been determined from observations. Since in the model calculations the amount of carbon available for grain condensation strongly influences the final outflow velocity of the wind (Arndt et al. 1997), we chose a photospheric carbon-to-oxygen ratio which produces an outflow velocity in agreement with the rather well determined observed value (cf. Table 2). The overabundance of carbon to oxygen of 1.38 adopted for the present model lies well within the range observed for cool bright carbon stars, i.e. those having an optical counterpart (e.g. Lambert et al. 1986). All other elements (including oxygen) are assumed to have solar abundances (Allen 1973).

The rather large value chosen for Δu was necessary to reproduce the observed amplitude of the light curves (see Sect. 4.4).

In order to model the observed far–infrared flux, the outer shell boundary was placed at $R = 2000\,R_0 = 1.1\,10^{17}$cm. The inner shell boundary is located well below the photosphere of the hydrostatic model at $r_i(t = 0) = r_0 = 0.91\,R_0$. During the calculation r_i varies sinusoidally around r_0 with amplitude $\Delta r_i = 0.14\,R_0$.

In Table 2 some quantities resulting from the evolved model are given together with respective observations. The entry "observation" refers to corresponding values found in the literature. Since these quantities usually are derived using different approaches (e.g. fitting rotational line profiles of different transitions in different molecules, using different underlying hydrodynamic, chemical, and/or radiative transfer models), these values are only indicative and might not be consistent among each other (cf. the excellent compilation of Loup et al. (1993)).

The value given in Table 2 for the mass loss rate, $\dot{M}$, is calculated by averaging the mass flux $4\pi r^2 \rho v$ through the outer boundary ($\sim 10^{17}$ cm) over a time interval $T = 15$P Similarly, the final outflow velocity v_∞ is obtained by averaging over T the velocity v at the outer boundary. The dust–to–gas mass ratio ρ_d/ρ_g is also obtained by averaging over T the ratio $m_C K_3/1.4 m_H n_{<H>} = 12K_3/1.4 n_{<H>}$ (cf. Eq. (2), m_C, m_H and $n_{<H>}$ denote the mass of a carbon atom, the mass of a hydrogen atom, and the total number density of hydrogen nuclei, respectively) at the outer boundary. Finally, the 2.2μm optical depth is obtained by averaging over T the optical depth at 2.2μm of the circumstellar shell calculated from the outer boundary to the stellar surface. Therefore, in all cases, the average value $< x >$ of a quantity $x(t)$ is determined from: $< x >= 1/T \int_{t-T}^{t} x(t')dt'$, with $T = 15P \sim 10^4$days or 30 years.

The average mass loss rate produced by the model is about a factor of 4 higher than the value typically derived by fitting CO rotational line observations (e.g. Knapp & Morris 1985, Sopka et al. 1989). In this type of investigations usually a constant outflow velocity and a constant CO/H_2 ratio is assumed. The uncertainty of these mass loss rates, apart from the distance uncertainty, is typically quoted to be about a factor of 2

Table 2. Resulting quantities of the evolved model

	$< \dot{M} >$ $[M_\odot \mathrm{yr}^{-1}]$	$< v_\infty >$ $[\mathrm{kms}^{-1}]$	$< \rho_\mathrm{d}/\rho_\mathrm{g} >$ 10^{-3}	$< \tau_{2.2\mu} >$	L_min $[L_\odot]$	L_max $[L_\odot]$	d kpc
model	$1.2\,10^{-4}$	14.7	1.9	18	9299	17320	1.2*
observation	$2.9\,10^{-5}$[a]	14.5[a]	4.5[b]	> 3.5[c]			0.57[a]–2.0[c]

* see Sect. 4.2; [a] Knapp & Morris (1985), ($\dot{M}$ scaled to d = 1.2kpc)
[b] Sopka et al. (1985); [c] Jones et al. (1978)

(e.g. Knapp & Morris 1985, Sopka et al. 1989). In our model, the mass loss rate results directly from the time–dependent hydrodynamics calculation for the expanding gas-dust mixture. To test whether this model is also able to explain the observed line profiles would require a non–LTE radiative transfer calculation in the respective molecular transitions, which is beyond the scope of the present paper.

The calculated average outflow velocity is in excellent agreement with the value derived from the observed width of the CO rotational line profiles. This agreement is mainly achieved by choosing a C/O ratio of 1.38. Since the average dust-to-gas ratio also is strongly dependent on the available amount of condensible carbon and thus on the C/O ratio (cf. Arndt et al. 1997), its value is in principle also determined by the velocity criterion. The model produces a dust-to-gas ratio, which is about a factor of 2 smaller than the commonly assumed value of about $4\,10^{-3}$. This latter value is derived from combining dust loss rates determined from submm observations with the gas loss rates derived from CO line profiles. In order to fit the submm dust emission, a value for the mass absorption coefficient of the dust component has to be assumed (e.g. Sopka et al. 1985). They choose a value for the mass absorption coefficient $\kappa_\nu(400\,\mu\mathrm{m}) = 20\mathrm{cm}^2\mathrm{g}^{-1}$ and argue that its uncertainty might be about a factor of 3. Since the equation relating the observed submm flux to the dust loss rate is linear in the mass absorption coefficient (their Eq. (3)), the uncertainty of $\kappa_\nu(400\,\mu\mathrm{m})$ also applies to the dust loss rate derived from this equation. In conclusion the dust-to-gas ratio produced in our model calculation is compatible with the values typically derived by other authors from observations.

4.1. Radial structure of the dust shell model

The radial structure of the CDS model is shown in Fig. 2 at t = 1.25 P corresponding to maximum phase of the light curves (cf. Fig. 5). Here and in the following, values for the instants of time are given relative to the initial time, from which on the light curves are plotted. This instant t = 0 P actually corresponds to t = 66 P if measured with respect to the hydrostatic initial model.

Similar to all our time–dependent models (as discussed e.g. in Paper I) several characteristic structures are also present in the current model:

– the CDS exhibits a discrete or onion–like structure, i.e. the dust is not distributed homogeneously but is concentrated in discrete layers. This can be seen, for instance, in the course of the degree of condensation f_c in the 2nd row of Fig. 2.

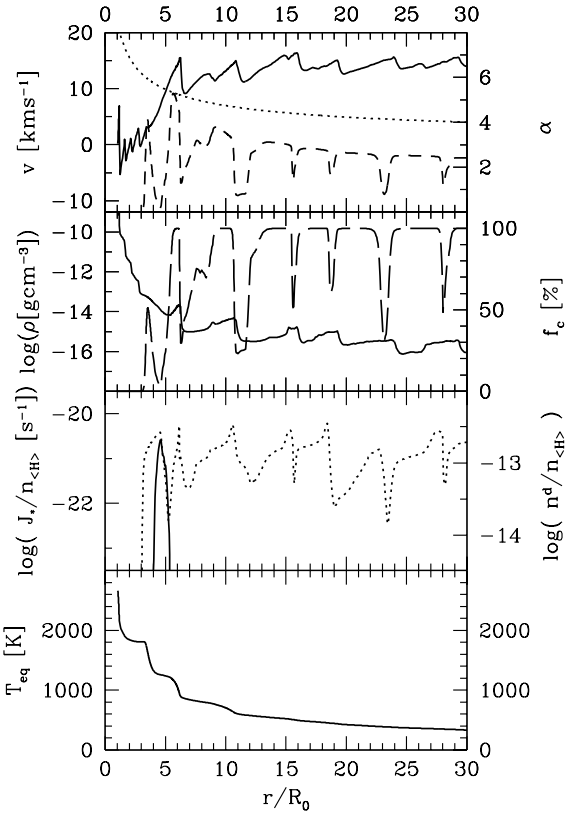

Fig. 2. Radial structure of the CDS at t = 1.25 P (cf. Fig. 5). Shown are **upper diagram:** the velocity u (solid line), escape velocity (dotted line), and radiative acceleration in units of the local gravitational deceleration α (dashed line), **2^{nd} diagram:** the density ρ (solid line) and the degree of condensation f_c (i.e. the fraction of condensible carbon actually condensed into grains) (dashed line), **3^{rd} diagram:** the nucleation rate $J_\star$, i.e. the number of dust particles formed per second and H-atom (solid line) and the number of dust particles per H–atom $n_\mathrm{d}/n_{<\mathrm{H}>}$ (dotted line), **lower diagram:** the equilibrium temperature T_eq. The normalization radius R_0 is the stellar radius of the hydrostatic initial model (R_0 = 5.5 10^{13} cm).

– these dust layers are spatially correlated with the hydrodynamic structure, e.g. the velocity, which suggests that the strong shocks propagating through the shell are accelerated by radiation pressure on dust. Indeed, the process of *dust–amplified shocks* as described in detail in Paper I is also at work in the model presented here.
– the radial structure of the temperature is characterized by a pronounced *back–warming effect*, i.e. the material located below the dust layers is heated due to thermal re–emission

of the energy absorbed by the dust grains in the short wavelength spectral region.

The consequence of this backwarming effect for the nucleation process can be seen from the sharp inner edge of the nucleation rate shown in the 3rd. row of Fig. 2 (solid line). The sharp onset of dust nucleation is caused by the steep temperature gradient between 3.5 and 4 R_0. However, as can be seen from the distribution of the number of dust particles $n_{\rm d}/n_{<H>}$ and the degree of condensation $f_{\rm c}$, a considerable amount of dust is in fact present at higher temperatures ($T \approx 1800$ K), i.e. inside the region of dust nucleation. These particles have been formed during a previous time interval at lower temperatures ($T \approx 1200$ K). The presence of particles at considerably higher temperatures is possible by the fact, that the dust grains, once they have formed, are quite stable against thermal evaporation (which occurs only at $T \approx 1900$ K) (for a detailed discussion see Gauger et al. 1990).

A further property of this model is the formation of new dust layers on time scales longer than the pulsation period. Also this behavior is common to our model calculations (we call this effect *multiperiodicity*) and is connected to the fact, that the CDS possesses an eigenperiod (see Fleischer et al. 1995). Multiperiodicity in particular leads to a modulation of the light curves (see Winters et al. 1994b and Sect. 4.4). The model presented here produces new dust layers on a time scale of approximately five pulsation periods (e.g. around $t = 0.60$ P and $t = 5.60$ P in Fig. 5). Within this time interval the grains present in the new layer successively grow when the material becomes compressed by subsequent shocks produced by the interior pulsation of the star (see Winters et al. (1995) for a more detailed discussion). Since the details of this intermediate growth process do not repeat exactly from cycle to cycle, the radial structure of the dust shell at a fixed instant of time and also the temporal evolution of the light curves are slightly irregular.

4.2. Spectral energy distribution

Fig. 3 depicts the calculated spectral energy distribution (SED) at light maximum (l.h.s.) and light minimum (r.h.s.). The corresponding near– and mid–infrared observations where obtained by Le Bertre (1992) (filled squares), Le Bertre et al. (1995) (filled triangles) at JD=2445955 (maximum, l.h.s. diagram) and at JD=2446219 (minimum, r.h.s. diagram), while the IRAS data (crosses) and sub–mm measurements (Sopka et al. (1985), open square; Groenewegen et al. (1993), open triangles) were obtained at different phases, i.e. they are the same in both diagrams. At the l.h.s. ordinate the calculated radiative flux through the outer shell boundary is given, while the r.h.s. ordinate gives the observed flux on earth. Neglecting interstellar extinction (see the discussion in Le Bertre et al. (1995)), we can derive the distance d to AFGL 3068 from pure geometrical dilution of the radiation energy

$$R^2 F_{\nu,\rm calc.} = d^2 F_{\nu,\rm obs.} \qquad (11)$$

which for our model yields a value of $d = 1200$ pc.

The overall agreement between calculated and observed SED at both phases is rather satisfactory, although the model produces somewhat too much flux below 5μm at maximum phase. A slightly better fit to the near–infrared fluxes was produced by a different model calculation with $M_\star = 0.9 M_\odot$ and identical values for the other parameters. In that model, however, the amplitude of the K light curve was noticeably larger than observed and also the outflow velocity in that model was slightly larger ($v_\infty = 15.1 {\rm kms}^{-1}$).

The outer shell boundary of the model presented in Fig. 3 is located at $R = 2000\, R_0 = 1.1\, 10^{17}$cm. Sopka et al. (1989) derived a value for the maximum extent of the circumstellar molecular envelope of $2\, 10^{17}$cm from CO(J=1–0) and HCN(J=1–0) rotational line profiles. Placing the outer shell boundary at this value (i.e. $R = 4000 R_0$, which at 1200 pc, corresponds to a beam of 24.5 arcsec) would enhance the calculated sub–mm flux at minimum light (r.h.s. diagram) to values just above those measured by Groenewegen et al. (1993) at phase 0.19, i.e. close to maximum, through a beam of 18.5 arcsec.

4.3. Spatial spectra

In Fig. 4 the calculated intensity profiles $I(p)$ of the dust shell model (upper two rows) and the resulting visibility functions $V(q)$ (lower row) are shown at different wavelengths for different instants of time. Columns b) and c) refer to the same maximum and minimum phase as in Fig. 3. The first instant – column a), $t = 0.60\, P$ – corresponds to a phase, when a new dust layer just starts to form (i.e. the optical depth through the shell is at minimum), and the last instant – column d), $t = 3.80\, P$ – belongs to a phase of maximum optical depth of the dust shell, caused by the newly formed layer.

At wavelengths larger than $\lambda \approx 5\mu$m, the current location of the dust layers is clearly indicated by steps (e.g. at $\lambda = 12\mu$m) or even intermediate maxima in the intensity profiles in the inner shell region (e.g. at $\lambda = 25\mu$m). These structures are caused by thermal emission of dust, concentrated in the discrete layers. The different shape of the intensity profiles (continuous at 2.2μm, steps at 12μm and intermediate maxima at 25μm) is caused by the different optical depths of the dust shell in radial direction, i.e. along the impact parameter $p = 0$ ($< \tau^{\rm d}_{2.2\mu} > \approx 18$, $< \tau^{\rm d}_{12\mu} > \approx 2.7$, and $< \tau^{\rm d}_{25\mu} > \approx 1.2$).

The visibility functions shown up to a spatial frequency of $q = 1.5\, 10^6\, {\rm rad}^{-1}$ in the lower row of Fig. 4 mainly contain information about the intensity distribution outside of approximately 140 milli–arcseconds. To get a more direct impression of the intensity profiles in this spatial region, we have included an enlarged cut of the profiles in the middle row of Fig. 4. In this distant part of the shell, the profiles are rather smooth, indicating that the discrete dust layers merge while traveling to larger distances from the star (see also Fig. 2). These smooth intensity distributions lead to the continuous course of the visibility functions within the interval of spatial frequencies plotted in Fig. 4.

In order to cover the range of spatial frequencies shown in Fig. 4 (up to $q = 1.5\, 10^6 {\rm rad}^{-1}$), interferometer baselines of

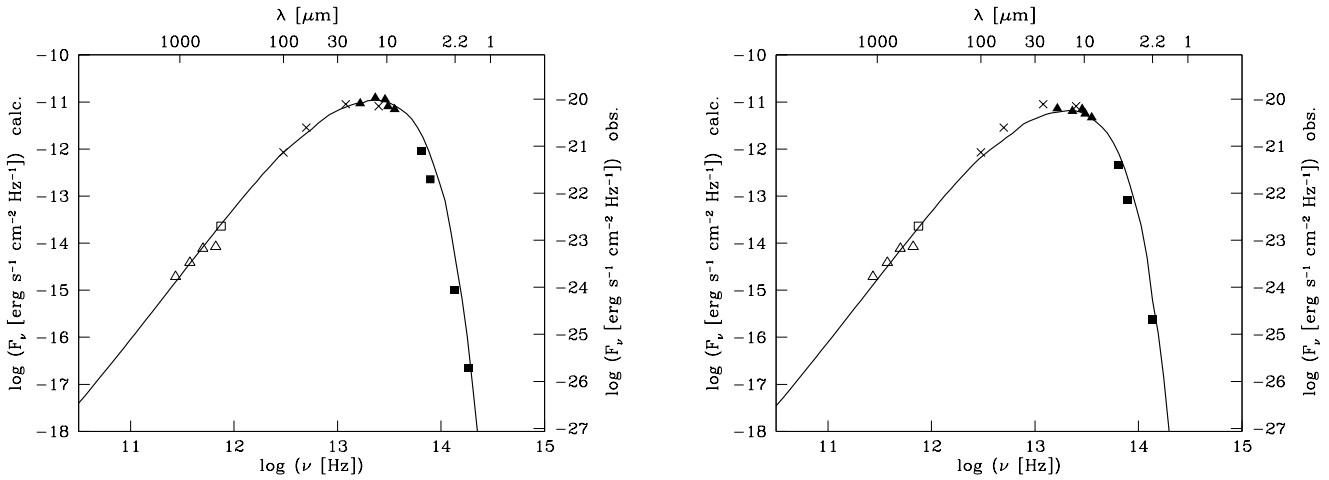

Fig. 3. Theoretical spectrum of the dust shell model (solid lines) at $t = 1.25P$ (l.h.s. diagram) and at $t = 2.80P$ (r.h.s. diagram), and observed spectrum of AFGL 3068 (symbols) at maximum phase of the light curve (JD=2445955, l.h.s. diagram) and at minimum phase of the light curve (JD=2446219, r.h.s. diagram)

3.3m, 18m and 37.5m are required at $\lambda = 2.2\mu$m, $\lambda = 12\mu$m, and $\lambda = 25\mu$m, respectively. The maximum spatial frequency shown in Fig. 4 approximately corresponds to the maximum baseline of the infrared spatial interferometer (ISI) described in Danchi et al. (1994), which operates at 11μm. Although AFGL 3068 has not been observed by these authors these figures demonstrate, that the resolution of currently available infrared interferometers is just at the limit of resolving a source like AFGL 3068.

A temporal evolution of the dust layers is clearly seen in the intensity profiles and also in the corresponding visibility functions, where the quantitative changes are however less pronounced. Therefore, in order to obtain a further test of the model, it would be very valuable to observe the temporal development of the intensity distributions of AFGL 3068 directly with very high angular resolution ($\approx$ 0.01 arcsec), e.g. by aperture synthesis techniques.

4.4. Light curves

The theoretical light curves at different wavelengths are shown in Fig. 5 for a time interval of 10 pulsation periods. These light curves clearly behave non-sinusoidal. Near–IR observations by Le Bertre (1992) and by Fouqué et al. (1992) at $\lambda = 2.2\mu m$, $\lambda = 3.8\mu m$, and $\lambda = 4.65\mu m$ are shown as open triangles. In addition, in the upper left diagram, the luminosity of the model is plotted, which shows a strictly sinusoidal variation. Hence, the modulation in the synthetic light curves is caused by circumstellar effects. In fact, this model is *multiperiodic*, which in this case means, that a new dust layer is formed approximately each 5 pulsation periods. A hint for this time scale can be drawn from tracing the deep minima at long wavelengths (e.g. $\lambda = 200\mu m$). Note further, while going from short to long wavelengths, that there is an inversion in the behavior of the synthetic light curves, i.e. an increase in the mean magnitude at short wavelengths turns into a decrease at longer wavelengths, and vice versa. This *inversion effect* is caused by the interaction of dust with the radiation field: the radiation energy absorbed by the grains at short wavelengths is thermalized and re-radiated at IR wavelengths. In reality, there might be a slight phase shift between the light curves at short and long wavelengths caused by the finite light travel time through the shell. This phase shift could at maximum amount to 0.12P (in the (unrealistic) extreme case, that the 200μm light curve completely originates from thermal emission of grains located at the far side outer boundary of the shell (see Wright & Baganoff 1995)) and is neglected here.

The data obtained by Le Bertre (1992) show that the light curves of AFGL 3068 cannot be approximated by a simple sine curve but that shifts in the mean magnitude are in fact observed for this object. Hence, the formation of discrete dust layers on time scales different from the pulsation period, which is a natural consequence of the model calculation, offers the possibility for a physical explanation of this observed behavior.

5. Discussion

5.1. Remarks on the light curves

At JD 2447785 (corresponding to t= 3.88P in Fig. 5) an exceptionally deep minimum in the light curves of AFGL 3068 was observed by Fouqué et al. (1992). Similarly deep minima were also found in the light curves of the carbon Mira R For (Feast et al. 1984, Le Bertre 1992), suggesting that the occurrence of regular long–term variations might be common to carbon–rich LPVs. Regular long–term variations are also present in the theoretical light curves of dynamical dust shell models (Winters et al. 1994b). Also in the model for AFGL 3068 presented here, we find a long term variation in the light curves (see Fig. 5). In the models, this behavior is caused by the formation of new dust layers on time scales longer than the pulsation period of the star. In our present calculation however, deep minima only occur at wavelengths shorter than $\lambda \approx 2\,\mu$m and longer than

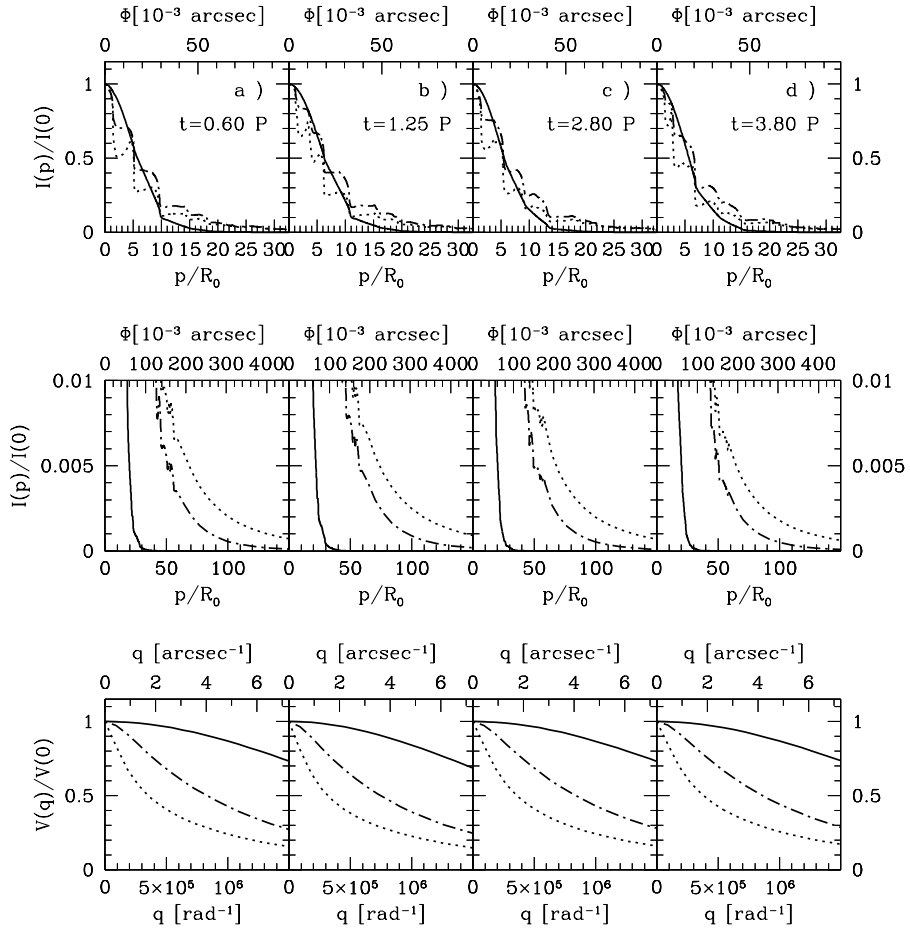

Fig. 4. Intensity profiles of the inner shell region (upper diagrams), of the outer shell region (enlarged, middle diagrams), and the corresponding visibility functions (lower panel) of the dust shell model for $\lambda = 2.2\mu$m (solid lines), $\lambda = 12\mu$m (dash–dotted lines), and $\lambda = 25\mu$m (dotted lines) at different instants of time (cf. Fig. 5). A distance of $d = 1200$ pc is assumed.

$\lambda \approx 25\mu$m, whereas the deep minimum for AFGL 3068 is observed at $\lambda = 2.2\,\mu$m, $3.8\,\mu$m, and $4.65\,\mu$m. This discrepancy might be due to inappropriate optical constants used here to describe the carbon grains and/or due to the neglect of the detailed size distribution function in the current calculation of the dust opacity. Both of these affect the wavelength dependence of the transport coefficients of the dust component and, therefore, influence the wavelength dependence of the synthetic light curves. In order to answer the question, whether the deep minimum observed in AFGL 3068 is at all caused by the formation of dust layers on time scales different from the pulsation time scale of the star, it is in the first place essential to detect further exceptionally deep minima in order to see whether the occurrence of deep minima is a recurrent phenomenon in this object. A continued monitoring of AFGL 3068 would therefore be very valuable.

5.2. Comparison with the model by Le Bertre et al. (1995)

In Fig. 6 the SED resulting from the model presented here is compared to the result of Le Bertre et al. (1995) at maximum phase of the light curve. Both models agree quite well at wavelengths between 2.2 and 100 μm, although the agreement between observation and calculation is slightly better for the Le Bertre et al. model between 2.2 and 10 μm. For $\lambda \geq 100\mu$m, the Le Bertre et al. model produces higher fluxes than the present one. This apparent difference between the models is mainly due to the different location of the outer shell boundary: Le Bertre et al. chose a distance of 3.74 10^{18} cm (i.e. 10^4 times their inner shell radius, for a distance of 1 kpc), while the outer boundary of the model discussed here is located at 1.1 10^{17} cm (i.e. 2000 times the initial stellar radius), thus much closer to the star. The measurements of Groenewegen et al. (1993) were obtained through a beam of 18.5 arcsec which translates to a radius of 1.4 10^{17} cm at 1 kpc (or 1.68 10^{17} cm at 1.2 kpc). Therefore, the measurements of Groenewegen et al. are in good agreement with the present model. However, in their Table 4, Le Bertre et al. show that their preferred model (with $Q \propto \lambda^{-1.3}$) agrees with the Groenewegen et al. data at 450 μm, but gives lower fluxes at $\lambda \geq 600\mu$m. They suggest that emission lines from the gas may contribute substantially to the observed sub–mm fluxes. On the basis of a spectral scan of a source similar to AFGL 3068 (IRC +10216), Groesbeck et al. (1994) argue that, for wavelengths longer than $\sim 750\mu$m, the molecular line emission may contribute to $\geq 50\%$ of the total flux in broadband measurements. Similar measurements on AFGL 3068 and at shorter wavelengths are highly desirable.

In Fig. 7 the temperature structures resulting from the model presented here are compared to the results of Le Bertre et al. (1995) at maximum and at minimum phase of the light curve.

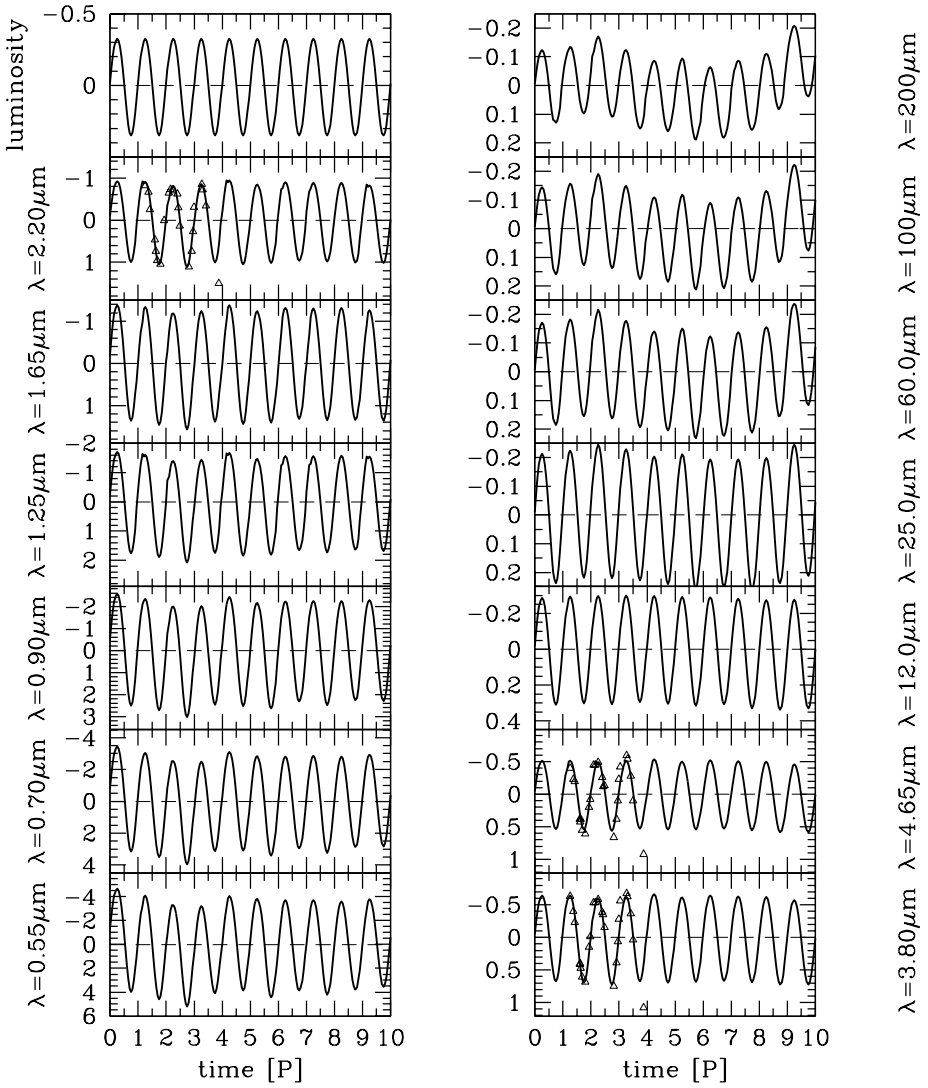

Fig. 5. Synthetic light curves of the dust shell model (solid lines) at different wavelengths over a time interval of 10 pulsation periods and observed light curves of AFGL 3068 (open triangles at λ = 2.20μm (K), λ = 3.80μm (L), λ = 4.65μm (M) (Le Bertre 1992). The light curves are plotted in magnitudes normalized to the mean magnitude. Note the different scaling of the ordinate at different wavelengths.

Very similar temperature structures result from both models in the outer part of the shell ($r > 15R_0$) at both phases. The inner shell boundary of the Le Bertre model is determined by an artificial "condensation temperature" of T_c = 930 K, whereas in the present calculation, where the process of dust condensation is treated in detail, dust already forms at temperatures around 1300 K (see Fig. 2), thus much closer to the star. As a result, the inner boundary of the Le Bertre et al. model is located in a region, where at least one dust layer is already present in the more detailed hydrodynamic model. Also, the temperature structure resulting from the consistent model calculation is much more complex in the inner shell region, where the dust actually forms. From this result we see that it is rather questionable whether a meaningful "dust condensation temperature" can be derived by means of parameterized radiative transfer models.

5.3. The assumption of the small particle limit

In the present model calculation we assume the small particle limit of Mie theory to calculate the transport coefficients of the grains. This assumption is justified, if the condition $(2\pi a/\lambda) \ll 1$ holds for all particle sizes present in the CDS at all wavelengths of interest (i.e. $\lambda > 1\,\mu$m for the present model). In order to check whether this assumption is valid for the model presented here, in this Section we discuss some aspects of the grain size distribution function resulting from the calculation.

In Fig. 8 the mean particle radius

$$< a >= \int a f(a) da \,/\, \int f(a) da \tag{12}$$

and the mean volume weighted particle radius

$$< a^3 >^{1/3} = \left\{ \int a^3 f(a) da \,/\, \int f(a) da \right\}^{1/3} \tag{13}$$

are shown. The volume weighted particle radius is the relevant quantity determining the extinction coefficient in the small particle limit (cf. Eqs. (1) and (2)) and thus would be derived as being the dominant particle size from a radiative transfer model based on the small particle limit. The fact that the calculated mean particle radius $< a >$ and the volume weighted mean particle radius $< a^3 >^{1/3}$ have rather similar values indicates that

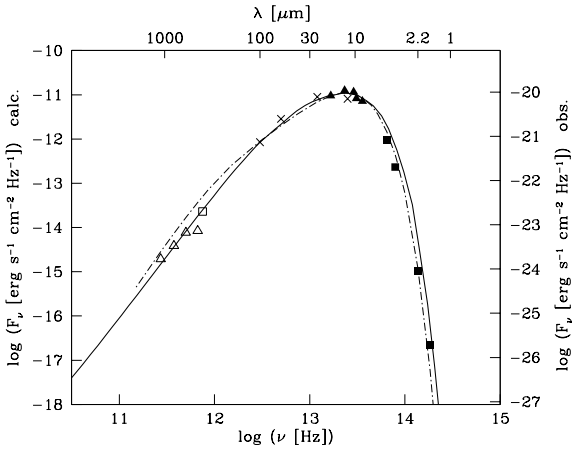

Fig. 6. Comparison between the SED resulting from the model presented here (solid line) with the SED resulting from the model of Le Bertre et al. (1995) (dash–dotted line) at maximum phase of the light curve (JD=2445955)

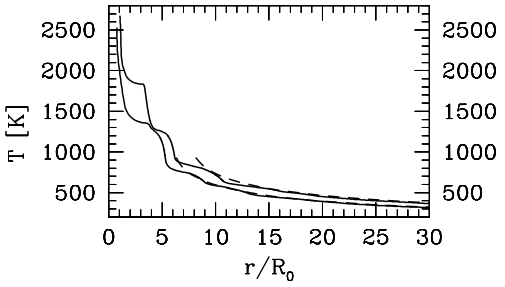

Fig. 7. Comparison between the temperature structure resulting from the model presented here (solid lines) and the temperature resulting from the model of Le Bertre et al. (1995) (dashed lines) at maximum phase of the light curve (t = 1.25 P, corresponding to JD=2445955, upper curves) and at minimum phase of the light curve (t = 2.80 P, corresponding to JD=2446219, lower curves)

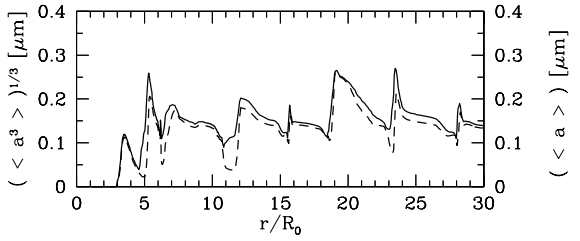

Fig. 8. Mean volume weighted particle radius (solid line) and mean particle radius (dotted line) at t = 1.25 P

the calculated grain size distribution function is sharply peaked around a dominant particle size. It can be seen from Fig. 8, that the mean particle radius is not constant in our model, but varies throughout the CDS. This apparent radial variation of the mean grain size results from the fact, that each gas element traveling through the circumstellar shell has its own history, leading to different size distributions in each of these elements. Within each element, the distribution function varies in time, according

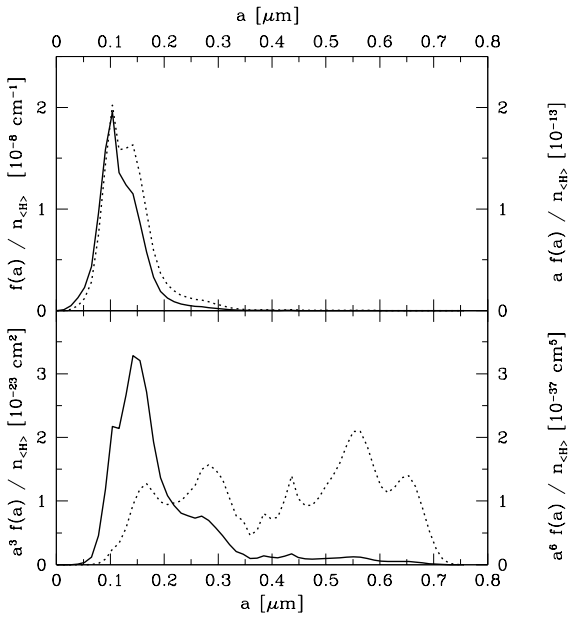

Fig. 9. Average particle size distribution function normalized to the total hydrogen density $n_{<\mathrm{H}>}$, weighted by different powers of the particle radius. Solid lines refer to the l.h.s. ordinate, dotted lines to the r.h.s. ordinate

to the formation of new grains in the inner part of the shell and to the subsequent growth of these nuclei.

The mean size distribution function in the outer region of the circumstellar shell is shown in the upper diagram of Fig. 9 (solid line, l.h.s. ordinate). The size distribution shown is an average of the local distribution functions in each volume element located between 30 and 60 R_0, i.e. in a region where the dust formation and growth process has ceased. Therefore, Fig. 9 represents the average size distribution function expected from the model calculation to be injected into the interstellar medium.

The distribution function looks rather narrow in the linear scaling chosen for Fig. 9, indicating that (on average) most particles have sizes around 0.1μm. However, there are in fact (few) larger particles. This is evident from the plots of the size–weighted distribution functions. From the lower panel of Fig. 9 one finds, that particles as large as 0.3 μm contribute to $a^3 f(a)$, i.e. the quantity determining the extinction coefficient in the small particle limit. The most important result is, however, that in the quantity $a^6 f(a)$ (which determines the scattering coefficient in the small particle limit, cf. Eq. (14)) not even a dominant particle size exists. On the contrary, all particles having sizes between 0.1 μm and 0.7 μm are of about equal importance for this quantity. The presence of polarization at λ = 2.2μm with degrees up to 30 % in the carbon–rich source IRC +10216 (Tamura et al. 1988) suggests that grains with size $a \geq \lambda/2\pi \sim 0.35\mu$m are formed in appreciable quantities around carbon stars. It is worth noting that our nucleation calculations fulfill this expectation.

Our theoretical result, that most particles have sizes of the order of 0.1μm, is also in accordance with estimates of the radial extent of the molecular emission from circumstellar dust shells.

Bujarrabal & Alcolea (1991) measured the extension of several CO envelopes with the 30-m IRAM telescope and derived typical values of some 10^{17}cm for the two carbon–rich shells of their sample. Loup (1991) has mapped the envelope of AFGL 3068 in the ^{12}CO(1-0) and ^{12}CO(2-0) rotational lines, also using the 30-m IRAM telescope. She obtained radii (HWHM) of 8-12 arcsec which translates to $R_{\rm CO} \approx 1.4\,10^{17} - 2.1\,10^{17}$cm for the distance of 1.2 kpc derived from the present investigation. Due to self-shielding against photo-dissociation by interstellar UV photons, emission by the CO molecule is supposed to be about 10 times more extended than the radial distribution of other molecules like C_2H_2, HCN, HC_3N, SiS, etc. (e.g. Cherchneff et al. 1993, Bujarrabal et al. 1994). Those molecules which are photo-dissociated typically reach a peak in their distribution around $\tau_{\rm UV} = 2$, where $\tau_{\rm UV}$ is the dust optical depth at $\lambda = 0.1\mu$m (e.g. Jura 1994). In our model, $\tau_{\rm UV} = 2$ is reached at $r \approx 350 R_0 = 1.9\,10^{16}$cm corresponding to an angular diameter of 2 arcsec, about a factor of 10 smaller than the measured CO distribution, as expected. Here, $\tau_{\rm UV}$ is calculated from the grain size distribution function, applying Mie theory for arbitrary particle sizes in order to calculate the extinction coefficient of the dust component.

On the other hand, Fukasaku et al. (1994), using the Nobeyama 45–m radio–telescope, have obtained line profiles for several molecules like CCH, C_4H, HC_3N, HC_5N, which are believed to be produced by photo–dissociation. The molecular shells are not resolved with this telescope. They model these line profiles by assuming shell diameters comparable to or smaller than the beam of the telescope (typically ~ 20 arcsec) and derive excitation temperatures and column densities for the corresponding molecules. Considering that with our model we predict for photo–dissociated species a diameter of ~ 2 arcsec, it would be very valuable to measure the extension of the molecular shells for several such species. Interferometric measurements in the millimeter range are now feasible with a resolution of $\sim$ 1 arcsec. Such measurements would provide a clear test of our modeling.

Since in the small particle limit the scattering coefficient is given by

$$\kappa_\nu^{\rm d,sca}(r) = \frac{128\pi^5}{3\lambda^4}\,{\rm Re}\left\{\frac{m(\nu)^2-1}{m(\nu)^2+2}\right\}\int a^6 f(a,r)da\,, \qquad (14)$$

and obviously particles as large as $0.7\,\mu$m significantly contribute to the integral, the assumption of the small particle limit is only valid for wavelengths $\lambda > 40\,\mu$m (corresponding to $2\pi a/\lambda < 0.1$). Since the photospheric spectrum (in frequency units) of our model peaks around $\lambda \approx 2\,\mu$m, the small particle limit is certainly not a good approximation for modeling light scattering even in the circumstellar dust shells around very cool long–period variables.

The next step for improving our model calculations therefore is of course the consideration of particles of arbitrary size and of the local size distribution function (instead of using only the moments of $f(a)$) in the determination of the transport coefficients of the dust component. In order to remain consistent with the hydrodynamic calculation, this step requires a consistent coupling between the hydrodynamic calculation and the detailed radiative transfer calculation. This coupling is necessary, since the transport coefficients resulting from the full size distribution function will probably lead to major changes in the radiative acceleration and in the equilibrium temperature stratification compared to the present situation, where both quantities result from the small particle limit.

5.4. Remarks on the assumption of spherical symmetry

In this paper we assume spherical symmetry of the central star and its circumstellar envelope. This assumption seems to be observationally justified at least for the outer regions of the circumstellar shells around AGB stars, but may become questionable in the very inner shell regions (e.g. Cohen 1990). As in these inner regions, due to the relatively high temperatures close to the star, mainly short wavelength radiation is involved, possible aspherical structures manifest themselves in the near infrared spectral region, influencing the observed energy distribution as well as the spatial brightness distribution (cf. Efstathiou & Rowan-Robinson (1990) and McCarthy et al. (1980), Ridgway & Keady (1988)).

Basically, there exist two different types of aspherical structures, which are caused by two basically different physical mechanisms. The first type is the more or less symmetric elliptical or disc–like structure, which is observed mainly for stars at the very end of their AGB evolution. Several mechanisms could be responsible for causing this kind of deviation from spherical symmetry, e.g. magnetic fields or the companion in a binary system, which would lead to a flattened or even disc–like structure of the circumstellar shell and could also cause a bipolar geometry of the outflows, as is observed during the transition of the progenitor star to the planetary nebula stage (e.g. Habing et al. 1989, Balick 1989). However, no consistent treatment of such an asymmetric system is at hand by now. A few attempts have been made to model the observed near infrared characteristics of non spherically symmetric shells, which are based on parameterized axisymmetric models (e.g. Lefèvre et al. 1983, Efstathiou & Rowan-Robinson 1990). These calculations however, do not include a reliable treatment of the involved physical mechanisms and, therefore, do not allow a real quantitative interpretation of these observations. On the other hand, based on a simple analytical model, Jura (1983) demonstrates, that important global quantities (such as the derived mass loss rate or the dissociation radii of the molecules) are not much affected by the assumption of an aspherical outflow as compared to a spherical model.

A quite different reason for producing an inhomogeneous shell structure in the case of a dusty outflow is provided by the process of dust formation itself: As the nucleation rate is an extremely steep function of the temperature, even modest temperature fluctuations can cause sudden dust formation within a well confined spatial region. This would lead to a clumpy (or cloudy) dust distribution, again especially in the inner parts of the shell, as is observed in some objects (e.g. Olofsson et al. 1992). The overall shell structure of these objects, as mapped in the CO

rotation lines, however, seems to be spherically symmetric to a high degree (cf. Olofsson et al. 1992). This conclusion also holds for the majority of the oxygen rich OH/IR stars, which were found from observations of the 1612 MHz OH maser line to give the overall impression of spherical symmetry (Habing et al. 1989).

6. Conclusions

We have presented the first consistent time–dependent model for the extreme carbon star AFGL 3068, including a detailed treatment of hydrodynamics, thermodynamics, dust formation, chemistry, and radiative transfer. This model is determined by the fundamental stellar parameters of the initial hydrostatic model: stellar mass $M_\star = 1\,M_\odot$, stellar luminosity $L_\star = 1.3\,10^4\,L_\odot$, stellar temperature $T_\star = 2200$ K, and carbon–to–oxygen abundance ratio $\epsilon_{\rm C}/\epsilon_{\rm O} = 1.38$. The pulsation of the star is simulated by a piston approximation at the inner boundary where the velocity varies sinusoidally with a period of $P = 696$ d and an amplitude of $\Delta u = 8\,{\rm km\,s^{-1}}$. This model produces a time averaged outflow velocity of $14.7\,{\rm km\,s^{-1}}$ and an average mass loss rate of $1.2\,10^{-4}\,M_\odot{\rm yr}^{-1}$. The resulting spectral energy distributions at minimum and maximum luminosity agree well with the observations. From a comparison between the calculated and the observed SEDs we derive a distance to AFGL 3068 of 1.2 kpc. The model also yields synthetic light curves whose amplitudes and non–sinusoidal temporal behavior are in good agreement with the observed light curves. The non–sinusoidal evolution of the synthetic light curves is caused by the formation of discrete dust layers on time scales longer than the pulsation time scale of the star. Since the formation of discrete dust layers also shows up in the synthetic brightness profiles of the model, we propose to perform high spatial resolution observations of the shell around AFGL 3068 in order to get a confirmation of the predicted dust formation mechanism.

The model presented here is calculated under the assumption of the small particle limit of Mie theory and light scattering by the dust grains is neglected. A few remarks on the size distribution function of the dust grains formed in the shell model are given. This discussion leads us to the conclusion, that the assumption of the small particle limit is at least not valid as far as light scattering is concerned. Therefore, our calculations are currently being improved by explicitly taking into account the size distribution function of the grains, resulting from our modeling approach. Since we expect a noticeable influence of the grain size distribution function on the transport coefficients of the dust component and thus on the resulting radiative acceleration and on the temperature structure, the improved version of the code will include a consistent coupling between hydrodynamic model calculation and the frequency–dependent radiative transfer calculation.

Acknowledgements. J.M.W. thanks K. Ketelsen (CRAY Research Inc.), who adapted and optimized the radiative transfer code for use on a T3D parallel computer, and thereby greatly improved the performance of the computations. The calculations were performed on the CRAY computers of the Konrad–Zuse–Zentrum für Informationstechnik Berlin and the HLRZ, Jülich. Subsequent data analysis has been performed on the WAP–cluster of the physics department of the TU Berlin. This work has been supported by the DFG (grant Se 420/8–1) and by the BMBF (grant 05 3BT13A 6). This research has made use of the SIMBAD database, operated at CDS, Strasbourg, France.

References

Allen C. W., 1973, Astrophysical Quantities, The Athlone Press, London
Arndt T. U., Fleischer A. J., Sedlmayr E., 1997, A&A submitted
Balick B., 1989, In Torres-Peimbert S., Planetary Nebulae, p. 83, Kluwer Academic Publishers, Dordrecht
Barnbaum C., Kastner J. H., Zuckerman B., 1991, AJ 102, 289
Bowen G. H., 1988, ApJ 329, 299
Bujarrabal V., Alcolea J., 1991, A&A 251, 536
Bujarrabal V., Fuente A., Omont A., 1994, A&A 285, 247
Cheeseman P., Stutz J., Self M., et al., 1989, Automatic Classification of Spectra from the Infrared Astronomical Satellite (IRAS) volume 1217 of NASA Reference Publication, NASA, Washington, DC
Cherchneff I., Glassgold A. E., Mamon G. A., 1993, ApJ 410, 188
Cohen M., 1979, MNRAS 186, 837
Cohen M., 1984, MNRAS 206, 137
Cohen R. J., 1990, In Mennessier M. O., Omont A., From Miras to Planetary Nebulae: Which path for stellar evolution?, p. 239, Editions Frontières, Gif sur Yvette Cedex - France
Danchi W. C., Bester M., Degiacomi C. G., Greenhill L. J., Townes C. H., 1994, AJ 107, 1469
Efstathiou A., Rowan-Robinson M., 1990, MNRAS 245, 275
Epchtein N., Le Bertre T., Lépine J. R. D., 1990, A&A 227, 83
Feast M. W., Whitelock P. A., Catchpole R. M., Roberts G., Overbeek M. D., 1984, MNRAS 211, 331
Fleischer A. J., Gauger A., Sedlmayr E., 1992, A&A 266, 321 (Paper I)
Fleischer A. J., Gauger A., Sedlmayr E., 1995, A&A 297, 543
Fouqué P., Le Bertre T., Epchtein N., Guglielmo F., Kerschbaum F., 1992, A&AS 93, 151
Fukasaku S., Hirahara Y., Masuda A., Kawaguchi K., Ishikawa S.-I., Kaifu N., Irvine W., 1994, ApJ 437, 410
Gail H.-P., Keller R., Sedlmayr E., 1984, A&A 133, 320
Gauger A., Gail H.-P., Sedlmayr E., 1990, A&A 235, 345
Gehrz R. D., 1989, In Allamandola L. J., Tielens A. G. G. M., Interstellar Dust, p. 445, Kluwer Academic Publishers, Dordrecht
Gehrz R. D., Hackwell J. A., 1976, ApJ 206, L161
Groenewegen M. A. T., Whitelock P. A., 1996, MNRAS 281, 1347
Groenewegen M. A. T., de Jong T., Baas F., 1993, A&AS 101, 513
Groesbeck T. D., Phillips T. G., Blake G. A., 1994, ApJS 94, 147
Habing H. J., te Lintel Hekkert P., van der Veen W. E. C. J., 1989, In Torres-Peimbert S., Planetary Nebulae, p. 359, Kluwer Academic Publishers, Dordrecht
Hashimoto O., 1995, ApJ 442, 286
IRAS Science Team, 1986, A&AS 65, 607
IRAS Science Team, 1988, IRAS catalogues and atlases, NASA RP–1190. NASA
Jones B., Merrill K. M., Puettner R. C., Willner S. P., 1978, AJ 83, 1437
Jura M., 1983, ApJ 275, 683
Jura M., 1986, ApJ 303, 327
Jura M., 1994, ApJ 434, 713
Justtanont K., Barlow M. J., Skinner C. J., et al., 1996, A&A 309, 612

Kastner J. H., Forveille T., Zuckerman B., Omont A., 1993, A&A 275, 163
Knapp G. R., Morris M., 1985, ApJ 292, 640
Lambert D., Gustafsson B., Eriksson K., Hinkle K. H., 1986, ApJS 62, 373
Le Bertre T., 1992, A&AS 94, 377
Le Bertre T., Gougeon S., Le Sidaner P., 1995, A&A 299, 791
Lefèvre J., Daniel J.-Y., Bergeat J., 1983, A&A 121, 51
Loup C., 1991, PhD thesis, Université J. Fourier - Grenoble I
Loup C., Forveille T., Omont A., Paul J. F., 1993, A&AS 99, 291
Lucy L. B., 1971, ApJ 163, 95
Lucy L. B., 1976, ApJ 205, 482
Maron N., 1990, Ap&SS 172, 21
McCarthy D. W., Howell R., Low F. J., 1980, ApJ 235, L27
Olofsson H., Carlström U., Eriksson K., Gustafsson B., 1992, A&A 253, L17
Omont A., Loup C., Forveille T., et al., 1993, A&A 267, 515
Ridgway S. T., Keady J. J., 1988, ApJ 326, 843
Sopka R. J., Hildebrand R., Jaffe D. T., et al., 1985, ApJ 294, 242
Sopka R. J., Olofsson H., Johansson L. E. B., Nguyen-Q-Rieu, Zuckerman B., 1989, A&A 210, 78
Tamura M., Hasegawa T., Ukita N., et al., 1988, ApJ 326, L17
Treffers R., Cohen M., 1974, ApJ 188, 545
Unno W., Kondo M., 1976, PASJ 28, 347
Whitelock P. A., Feast M. W., Catchpole R. M., 1991, MNRAS 248, 276
Winters J. M., Dominik C., Sedlmayr E., 1994a, A&A 288, 255
Winters J. M., Fleischer A. J., Gauger A., Sedlmayr E., 1994b, A&A 290, 623
Winters J. M., Fleischer A. J., Gauger A., Sedlmayr E., 1995, A&A 302, 483
Wright E. L., Baganoff F. K., 1995, ApJ 440, 322

This article was processed by the author using Springer-Verlag LaTeX A&A style file *L-AA* version 3.